Research Article

Irradiation behaviors of two novel single-phase bcc-structure high-entropy alloys for accident-tolerant fuel cladding

Zijian Zhang [a,b], En-Hou Han [a,*], Chao Xiang [a,c]

[a] Key Laboratory of Nuclear Materials and Safety Assessment, Institute of Metal Research, Chinese Academy of Sciences, Shenyang, 110016, China
[b] School of Materials Science and Engineering, University of Science and Technology of China, Shenyang, 110016, China
[c] School of Materials Science and Engineering, Northeastern University, Shenyang, 110819, China

ARTICLE INFO

ABSTRACT

High-entropy alloys (HEAs) are potential alternative materials for accident-tolerant fuel cladding due to their excellent irradiation resistance and high-temperature corrosion resistance. In this work, two novel body-centered cubic (bcc) structured $Mo_{0.5}NbTiVCr_{0.25}$ and $Mo_{0.5}NbTiV_{0.5}Zr_{0.25}$ HEAs were fabricated. Helium-ion irradiation was performed on the two HEAs to simulate neutron irradiation, and the crystal structure, hardness, and microstructure evolution were investigated. The crystal structure of the $Mo_{0.5}NbTiVCr_{0.25}$ HEA remained stable at low fluences, while amorphization may occur at high fluences in the two HEAs. The irradiation hardening value of the $Mo_{0.5}NbTiVCr_{0.25}$ was 0.77 GPa at fluences of 1×10^{17} ions/cm^2 and 1.49 GPa at fluences of 5×10^{17} ions/cm^2, while the hardening value of the $Mo_{0.5}NbTiV_{0.5}Zr_{0.25}$ was 1.36 GPa at ion fluences of 5×10^{17} ions/cm^2. In comparison with most of the conventional alloys, the two HEAs showed slight irradiation hardening. The helium bubbles and dislocation loops with small size were observed in the two HEAs after irradiation. This is the first time to report the formation of a dislocation loop in bcc-structure HEAs after irradiation. However, voids and precipitates were not observed in the two HEAs which could be ascribed to the high lattice distortion and compositional complexity of HEAs. This research revealed that the two HEAs show outstanding irradiation resistance, which may be promising accident-tolerant fuel cladding materials.

© 2021 Published by Elsevier Ltd on behalf of The editorial office of Journal of Materials Science & Technology.

1. Introduction

The fuel cladding in reactor pressure vessel services in a harsh environment of high-temperature corrosion and neutron irradiation can quickly lead to material degradation and even failure [1–3]. Following the adoption of light water reactor (LWR) as the main industrial design for electricity production in the 1950s, Zr-based alloys were commonly used as fuel cladding in water-cooled nuclear reactors because of their low thermal neutron absorption cross-section, excellent thermal conductivity, high melting point, and good corrosion resistance [4,5]. However, the Zr-based alloys may suffer from high-temperature steam oxidation and hydrogen pick-up at temperature above 1200 °C [6]. Furthermore, the high affinity of zirconium with hydrogen can result in the precipitation of hydrides and consequently induce significant embrittlement [7,8]. The issue of service security of Zr-based alloy has been arisen by the Fukushima Daiichi accident happening in 2011. There-

fore, accident tolerant fuel (ATF) should be urgently developed for responding to two extreme bounding accidents including reactivity insertion accident (RIA) and loss-of-coolant accident (LOCA) [9]. It is proposed to develop and deploy (1) an improved Zr-based alloy or coated zircaloy for the fuel cladding, (2) alternative cladding materials with better accident tolerance, and (3) alternative fuels with enhanced accident tolerance [10].

Recently, monophasic and multiphasic alloys consisting of multiple principal elements, called high-entropy alloys (HEAs) or complex concentrated alloys (CCAs), have received tremendous significance due to their unique microstructures and excellent properties [11,12]. HEAs typically consist of five to thirteen major elements with an atomic concentration between 5 % and 35 % for each element [13,14]. Unlike classical alloys, HEAs exhibit higher mixing entropy that can suppress the formation of ordered intermetallic compounds and promote the formation of simple solid solutions with face-centered cubic (fcc), body-centered cubic (bcc), and hexagonal close-packed (hcp) structure [13–16]. Many studies have suggested that HEAs possess excellent mechanical properties [17–19], corrosion resistance [20–23], thermal stability [24–26], wear resistance [27–29], and irradiation resistance [30–32]. There-

fore, the HEAs have become promising candidates satisfying the critical requirements of complex environments for ATF cladding.

The principal effects of irradiation on conventional alloys include non-equilibrium segregation, physical changes to the microstructure (dislocation loops, dislocation network, voids, bubbles, precipitates), and hardening [33]. These effects of irradiation can cause material degradation and even failure. Recently, there have been some studies about the irradiation of HEAs, which show great irradiation resistance due to their severe lattice distortion and high atomic-level stress [34]. For example, Yang et al. [31] investigated irradiation tolerance of the fcc-structure CrMnFeCoNi HEA, which showed the most stable structure and the best helium-ion irradiation tolerance at both room temperature and 450 °C, as compared with 304 stainless steel and pure Ni. However, the CrMnFeCoNi HEA may be unsuitable to nuclear material for Co element that can transform to radioactive ^{60}Co after absorption of the neutron. Moreover, the Mn element with a high thermal neutron absorption cross-section can reduce neutron utilization. Kumar et al. [30] reported that the fcc-structure FeNiMnCr HEA exhibited superior radiation resistance than conventional austenitic alloys such as stainless steels. Nevertheless, literature-reported irradiation-resistant HEAs were limited to those with single fcc structure. The irradiation behavior of bcc-structure HEAs has been rarely investigated. Lu et al. [32] reported a single-phase bcc-structure $Ti_2ZrHfV_{0.5}Mo_{0.2}$ HEA possessing excellent irradiation resistance, i.e. scarcely irradiation hardening and abnormal lattice constant reduction after helium-ion irradiation. Moschetti et al. [35] studied room-temperature mechanical properties of the ion-irradiated TiZrNbHfTa HEA, which showed excellent damage-tolerant properties with good combinations of strength and ductility both before and after ion irradiation. However, the study only paid attention to helium bubbles, but other changes to microstructure were not investigated. The previous literature about irradiation-induced microstructure evolution of bcc-structure HEAs was insufficient.

Considering the selection of the element and structure of HEA, elements with low thermal neutron absorption cross-section and thermal conductivity are introduced to design HEAs to ensure high uranium resource utilization and formation of bcc structure. Xiang et al. [36] have recently designed and prepared two bcc-structure MoNbCrVTi and MoNbCrZrTi HEAs composed of alloying elements with low thermal neutron absorption cross-section and high thermal conductivity. The density, hardness, microstructure, and compressive mechanical properties of the two HEAs were preliminarily investigated. They also researched corrosion resistance of $Mo_{0.5}VNbTiCr_x$ HEAs, which exhibited greater corrosion resistance than Zr-4 alloy in superheated steam [37]. However, the irradiation resistance of the promising $Mo_{0.5}VNbTiCr_x$ HEAs has not been investigated, which is of paramount importance for ATF cladding materials.

In the present work, two novel bcc-structure $Mo_{0.5}NbTiVCr_{0.25}$ and $Mo_{0.5}NbTiV_{0.5}Zr_{0.25}$ HEAs with elements of low thermal neutron absorption cross-section and high thermal conductivity were prepared. Helium-ion irradiation was performed on the two HEAs to simulate neutron irradiation. The crystal structure, hardness, and microstructure evolution induced by irradiation were investigated. This work provided systematic irradiation behaviors, especially changes of the microstructure of two novel bcc-structure HEAs.

2. Experimental

2.1. Material

Two alloy ingots of $Mo_{0.5}NbTiVCr_{0.25}$ and $Mo_{0.5}NbTiV_{0.5}Zr_{0.25}$ were fabricated by using commercially pure elements (higher than

Table 1
Nominal compositions (at.%) of the Cr-HEA and Zr-HEA.

HEAs	Cr	Mo	Nb	Ti	V	Zr
Cr-HEA	6.66	13.33	26.67	26.67	26.67	–
Zr-HEA	–	15.38	30.77	30.77	15.38	7.70

99.5 wt%) in a water-cooled copper crucible of vacuum arc furnace under Ti-gettered argon atmosphere. For convenience, the two HEAs were designated as Cr-HEA and Zr-HEA, respectively. Each ingot was flipped-over and re-melted at least five times to ensure chemical homogeneity. The weight of each ingot was about 100 g, and the dimension was approximately 44 mm in diameter and 10 mm in height. All the alloy ingots were hot isostatic pressed at 1200 °C and 150 MPa for 2 h to reduce the solidification porosity, followed by annealing treatment at 1200 °C for 72 h (Cr-HEA) or 24 h (Zr-HEA). Before annealing treatment, the specimens were sealed in quartz tubes backfilled with high purity argon. The nominal compositions of the Cr-HEA and Zr-HEA are listed in Table 1.

2.2. Helium-ion irradiation

Specimens with a dimension of 7 mm × 7 mm × 1 mm were cut from the central parts of the alloy ingots. They were ground using SiC papers up to 3000 grit, and then mechanically polished using diamond pastes of 1.5 μm and 0.5 μm. Finally, specimens were polished by 40-nm colloidal silica slurry for over 2 h to move the residual strain induced by grinding and mechanical polishing.

All the irradiation experiments were carried out at the 320 kV platform for multi-discipline research with highly charged ions at the Institute of Modern Physics, Chinese Academy of Sciences. The Cr-HEA specimens were irradiated with 400 keV He^{2+} at 350 °C up to ion fluences of 1×10^{17} ions/cm^2 and 5×10^{17} ions/cm^2, and the Zr-HEA specimens were irradiated with 400 keV He^{2+} at 350 °C up to ion fluences of 5×10^{17} ions/cm^2. The effect of irradiation influence on the microstructure of Cr-HEA can be investigated by comparison of Cr-HEA with low and high fluences. At the same time, the irradiation resistance of the two alloys can be evaluated by comparison of Cr-HEA and Zr-HEA with high fluences. The depth damage profile was calculated by the Stopping and Range of Ions in Materials 2008 (SRIM 2008) software, as shown in Fig. 1. The peak irradiation doses induced by helium collision are approximate 2.1 and 10.5 dpa (displacements per atom) at 900 nm for fluences of 1×10^{17} ions/cm^2 and 5×10^{17} ions/cm^2, respectively. The irradiation damage extends to a maximum depth of ~1100 nm for both fluences.

2.3. Microstructure characterization and nanoindentation test

Microstructure and composition analyses were carried out by X-ray diffraction (XRD), scanning electron microscopy (SEM), and transmission electron microscopy (TEM). The XRD analyses were performed at a voltage of 40 kV and a current of 40 mA. The TEM specimens were prepared by Helios 600i focused ion beam (FIB), and the volumes containing a grain boundary were lift out vertically the Ga-ion beam. The low energy of 2 keV was used at the last thinning stage to minimize the irradiation damage induced by Ga ions. TEM observations were performed at 200 kV using JEM-2100 F equipped with an energy dispersive X-ray spectroscope (EDX). Microhardness was measured using nanoindentation (Agilent G200) with a Berkovich diamond indenter. The indention depths were in the range of 50–110 nm, and at least 10 measurements for each specimen were performed to gain an average value of microhardness.
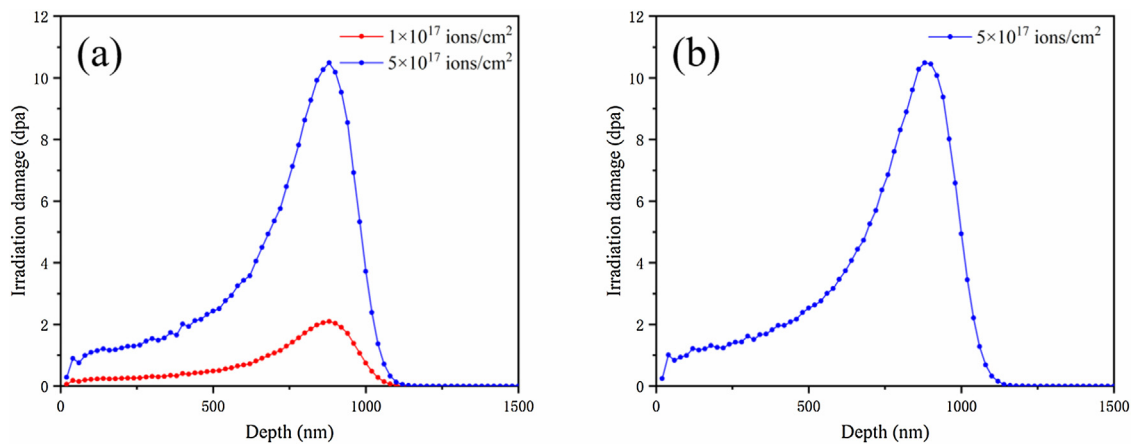
Fig. 1. The depth damage profiles of the Cr-HEA (a) and Zr-HEA (b) as-calculated by SRIM 2008 computer software.
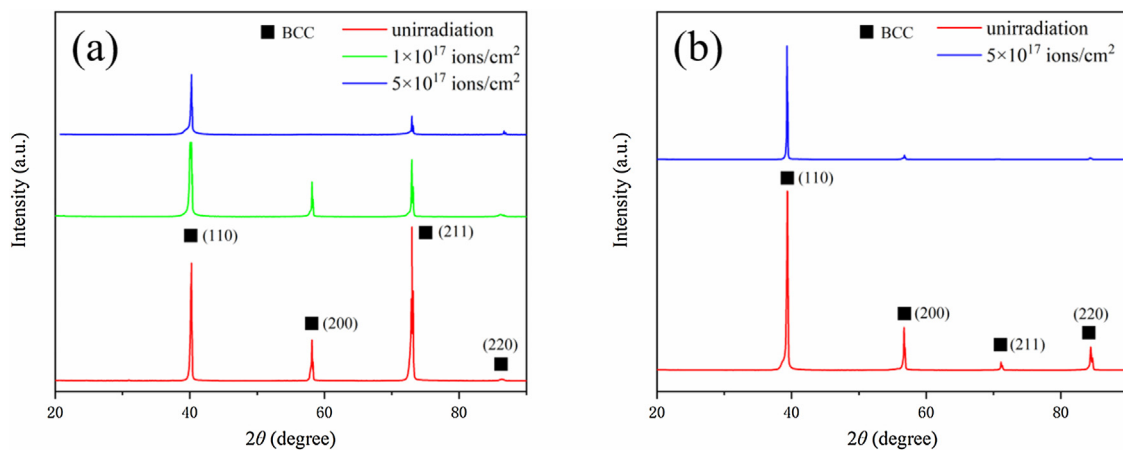

Fig. 2. (a) XRD patterns of the unirradiated and irradiated Cr-HEA at ion fluences of 1×10^{17} ions/cm^2 and 5×10^{17} ions/cm^2. (b) XRD patterns of the unirradiated and irradiated Zr-HEA at ion fluences of 5×10^{17} ions/cm^2.

3. Results and discussion

3.1. Microstructure of the unirradiated HEAs

The XRD patterns of the unirradiated Cr-HEA and Zr-HEA are shown in Fig. 2, which indicate that the two HEAs both have a single bcc structure with a lattice constant of 3.165 Å and 3.250 Å, respectively. Using the nominal composition of the two HEAs and lattice constant of the pure metals, the lattice constant of the disordered bcc solid solutions could be calculated by the rule of mixtures [38]:

$$a_{mix} = \sum_{i=1}^{n} c_i a_i \qquad (1)$$

where a_i and c_i are the lattice constant and atomic fraction of element i, respectively. The calculated lattice constants are 3.172 Å and 3.248 Å for the Cr-HEA and Zr-HEA, respectively. The similar values of the experimental and calculated lattice constants indicate that the two HEAs are composed of disordered solid solution phase. As shown in Fig. 3, the SEM images show that the two HEAs both have equiaxed microstructure with grain size of 100–200 μm.

TEM observation was performed on the two unirradiated HEAs to obtain more detailed information about microstructure. The selected area electron diffraction (SAED) patterns in Fig. 4 show that both Cr-HEA and Zr-HEA have a single bcc structure without a second phase, which is consistent with the XRD results. As shown in Fig. 5(a) and (b), the bright-field (BF) and dark-field (DF) images

suggest that there are some elongated precipitates with the width of ~20 nm at the grain boundary of the Cr-HEA. Fig. 5(c) shows a high-resolution TEM image of the precipitate and the corresponding fast Fourier transformation (FFT) pattern, which displays an fcc structure. The EDX line scanning across the precipitates can be seen in Fig. 5(d), and the maximum Ti content reaches as high as ~60 at.%. Long et al. [39] reported that the TiO phase with fcc structure was formed in the NbMoTaWVTi refractory HEA due to the O doping during the preparation process. In consideration of composition and structure, the Ti-rich precipitates may be Ti (C, N, O) phase, which was ascribed to the pick-up of C, N, or O during the preparation process. Some precipitates are also observed at the grain boundary of the Zr-HEA, as shown in Fig. 6(a) and (b). The high-resolution TEM image and the corresponding FFT pattern (Fig. 6(c)) of the precipitates exhibit an fcc structure, and the EDX line scanning (Fig. 6(d)) across the precipitates show that the maximum Zr content reaches as high as ~35 at.%. Zr element has the highest electronegativity in the Zr-HEA, which is most likely to combine with the non-metallic element. The fcc-structure Zr-rich precipitates may be Zr (C, N, O) phase due to the pick-up of C, N, or O during the preparation process.

3.2. XRD analysis of the irradiated HEAs

XRD tests were performed to investigate the irradiation effect on the crystal structure of the Cr-HEA and Zr-HEA, which are shown in Fig. 2. The Cr-HEA exhibits a bcc structure with (110) and (211) planes preferred orientation. After irradiation to fluences of
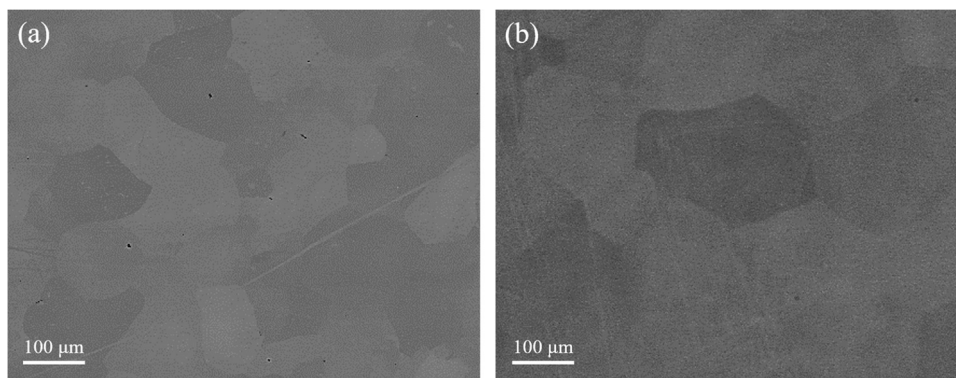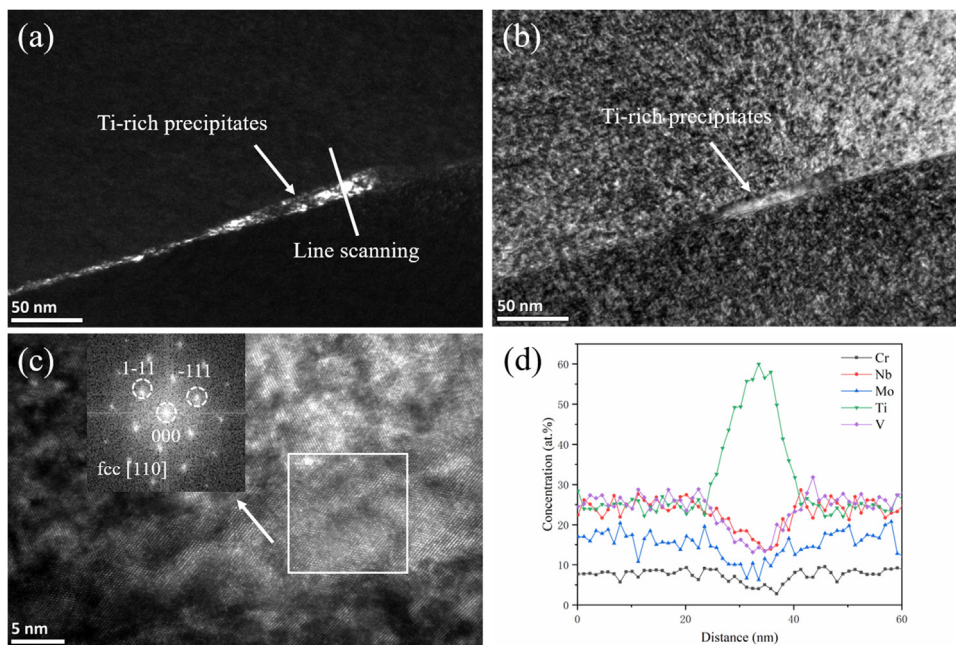
Fig. 3. SEM backscatter electron images of the unirradiated Cr-HEA (a) and Zr-HEA (b). The two HEAs both have an equiaxed microstructure with the grain size of 100–200 μm.
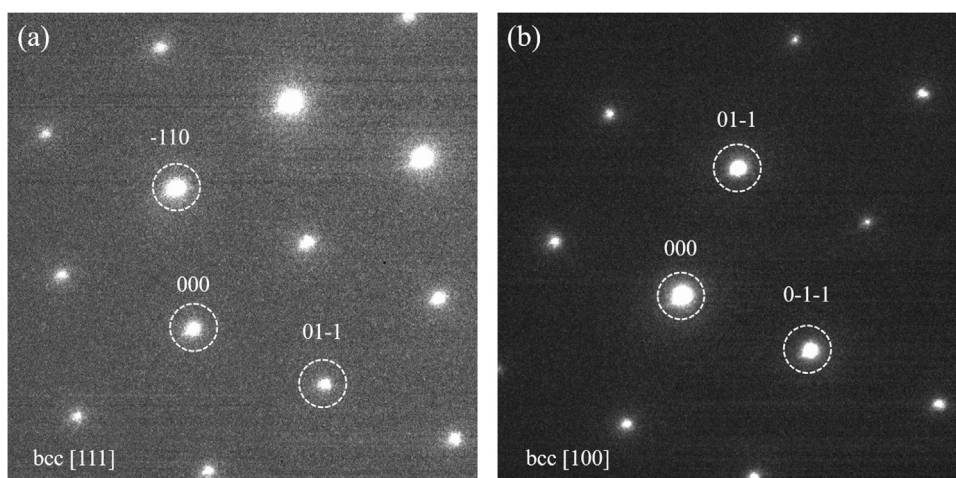

Fig. 4. SAED patterns of the unirradiated Cr-HEA (a) and Zr-HEA (b). The two HEAs both show a single bcc structure.

Fig. 5. DF image (a), BF image (b), high-resolution image (c), and EDX line scanning (d) of Ti-rich precipitates in the unirradiated Cr-HEA.

1×10^{17} ions/cm², the Cr-HEA remains stable bcc structure without intermetallic phase. However, the intensity of bcc diffraction peaks beside the (110) plane decreases dramatically and can hardly be identified as the Cr-HEA is irradiated to fluences of 5×10^{17} ions/cm². On the other hand, the Zr-HEA exhibits a bcc structure with (110) plane preferred orientation. After irradiation to fluences
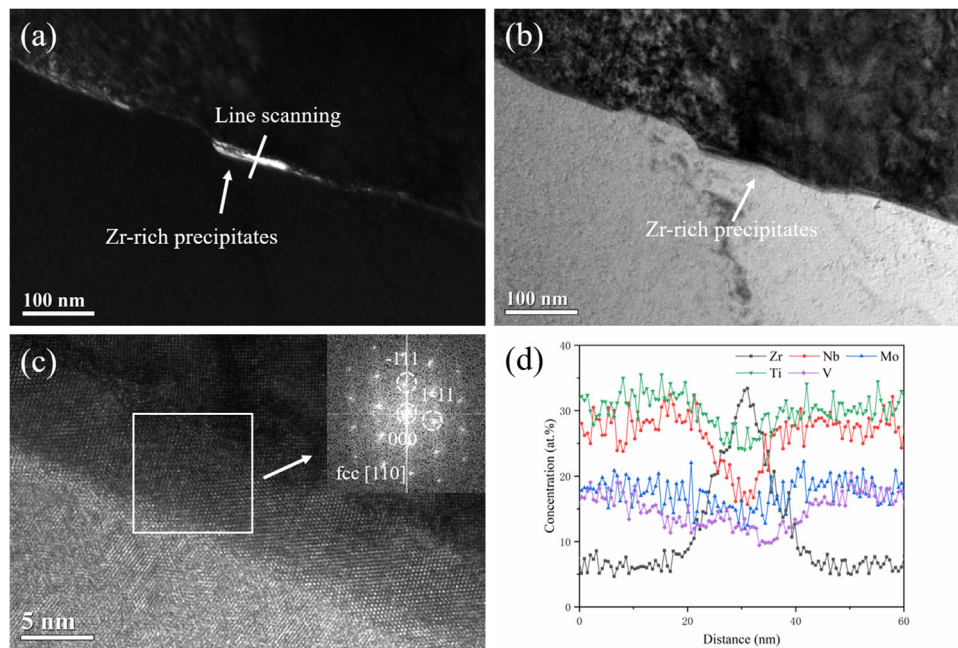
Fig. 6. DF image (a), BF image (b), high-resolution image (c), and EDX line scanning (d) of Zr-rich precipitates in the unirradiated Zr-HEA.

of 5×10^{17} ions/cm^2, the intensity of bcc diffraction peaks beside the (110) plane decreases dramatically and even disappears. Sun et al. [40] reported that the Al$_{1.5}$CrFeNi HEA film had a bcc structure which was broken down after helium-ion irradiation. They observed the dramatically decreasing intensity of bcc diffraction peaks in the irradiated films, and the diffraction peaks could hardly be distinguished. Moreover, Jiang et al. [41] studied the influence of ion irradiation on Zr-4 alloy, and the intensity of XRD peaks was gradually weakening with increasing the irradiation, which may be ascribed to the amorphization induced by irradiation. In this work, the decreases of the diffraction peaks may be ascribed to the formation of the amorphous structure due to high atomic-level stress. However, the local melting and recrystallization of amorphous structures will occur due to thermal spikes induced by irradiation [42].

There is no angle shift in XRD patterns of the irradiated HEAs in comparison with those of the unirradiated HEAs, which means that the lattice constants have no obvious change after ion irradiation. Zhang et al. [26] investigated the irradiation response of the CoCrCuFeNi HEA, which had an increasing lattice constant with an average dose from 0.73–368.5 dpa. On the contrary, Lu et al. [32] observed the decrease of lattice constant in the Ti$_2$ZrHfV$_{0.5}$Mo$_{0.2}$ HEA after irradiation dose of 3×10^{16} ions/cm^2. However, the lattice constants of the two HEAs have no obvious change in this work, which exhibits a stable crystal structure after irradiation. There are two possible reasons that (1) irradiation can hardly influence the lattice constant of HEAs due to small-size defects induced by irradiation, and (2) irradiation can result in a negligible change of lattice constant, which can rarely be identified by XRD.

3.3. Irradiation hardening

A common empirical rule suggests that substrate independent measurements can be obtained if the indentation depth is less than one-tenth of the film thickness [43]. Therefore, the maximum indentation depth is controlled at 110 nm that is one-tenth of the irradiation damage depth to avoid the substrate effect. Moreover, the measurement results of less than 50 nm are excluded for eliminating the effects of residual stress on the specimen surface. The
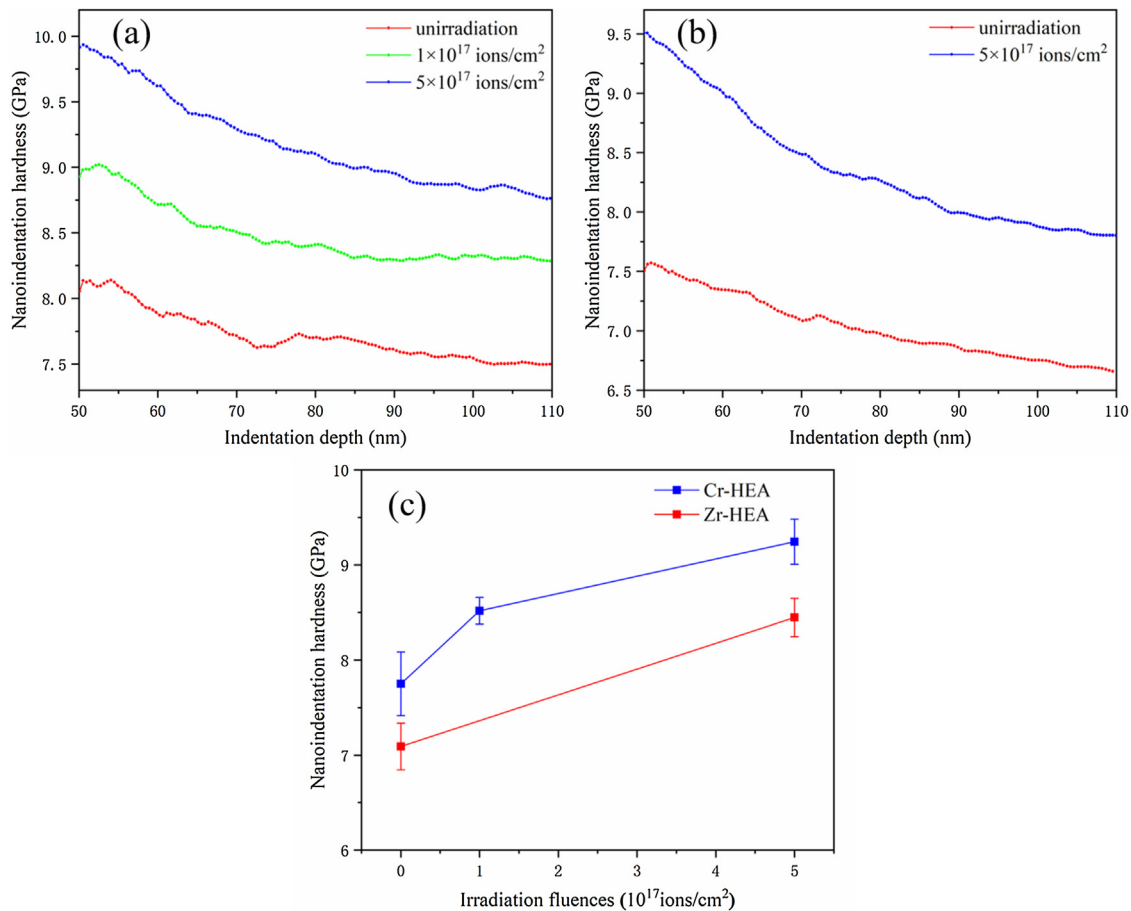
nanoindentation hardness is plotted as a function of the depth in unirradiated and irradiated Cr-HEA, as shown in Fig. 7(a). The results show obvious irradiation hardening, and the higher irradiation fluence causes the larger hardening. Fig. 7(b) shows that the irradiated Zr-HEA has a larger hardness than the unirradiated Zr-HEA.

The average nanoindentation hardness is regarded as the hardness of each specimen for the quantitative evaluation of irradiation hardening, and the calculation method is averaging all hardness test values at the depth range from 50 to 110 nm for each specimen. The irradiation hardening value (ΔH) can be described as the difference of the average nanoindentation hardness between the unirradiated and irradiated HEAs. Fig. 7(c) shows that the average nanoindentation hardness (H_0) is plotted as a function of the irradiation fluence. Moreover, the results of average nanoindentation hardness are summarized in Table 2. Compared with the unirradiated Cr-HEA (7.75 GPa), the hardness reaches 8.52 GPa at fluences of 1×10^{17} ions/cm^2, and then increases to 9.24 GPa at fluences of 5×10^{17} ions/cm^2. However, the hardness of the Zr-HEA has a change from 7.09 GPa to 8.45 GPa at fluences of 5×10^{17} ions/cm^2. The Cr-HEA exhibits slightly larger irradiation hardening than the Zr-HEA at high fluences.

The irradiated induced hardening and embrittlement is one of the main failure modes of structural materials in nuclear power plants [44]. Irradiation hardening of numerous nuclear alloys has been studied in different irradiation conditions [41,45–48]. For example, Bai et al. [47] studied hardening of the RPV steel irradiated to 10 dpa using 3.5 MeV Fe ions, which showed increasing hardness from 12.3–20.1 GPa. In comparison with most of the conventional alloys, the two HEAs exhibit less hardening, which may be ascribed to fewer defects induced by irradiation in HEAs.

3.4. Irradiation defects

As shown in Fig. 8, considerable small white spots can be observed, which represent helium bubbles. It can be seen from Fig. 8(a)–(c) that the sizes of bubbles are approximate 1–3 nm in the three irradiated specimens. Furthermore, the bubble density may be slightly different, which is beyond the sensitivity of TEM obser-

Fig. 7. (a) Nanoindentation hardness as a function of the indentation depth in the unirradiated and irradiated Cr-HEA at ion fluences of 1×10^{17} ions/cm^2 and 5×10^{17} ions/cm^2. (b) Nanoindentation hardness as a function of the indentation depth in the unirradiated and irradiated Zr-HEA at ion fluences of 5×10^{17} ions/cm^2. (c) Average nanoindentation hardness as a function of the irradiation fluence in the unirradiated and irradiated Cr-HEA and Zr-HEA.

Table 2
Nanoindentation test results (GPa) of the Cr-HEA and Zr-HEA.

HEAs	Unirradiated	1×10^{17} ions/cm^2		5×10^{17} ions/cm^2	
	H_0	H_0	ΔH	H_0	ΔH
Cr-HEA	7.75 ± 0.33	8.52 ± 0.14	0.77 ± 0.47	9.24 ± 0.24	1.49 ± 0.57
Zr-HEA	7.09 ± 0.25	–	–	8.45 ± 0.20	1.36 ± 0.45

vation due to extremely dense distribution. Fig. 8(d) and (e) shows high-magnification BF images of the helium bubbles in Cr-HEA and Zr-HEA irradiated to fluences of 5×10^{17} ions/cm^2, respectively. Numerous bubbles are presented in the interior grains and at the grain boundary. The formation of a helium bubble is usually observed in conventional alloys performed by helium-ion irradiation. Lei et al. [49] reported the formation of helium bubbles with a size of 1.94–5.66 nm in UNS N10003 alloy irradiated to 6.18 dpa. Liu et al. [50] studied the evolution of helium bubbles in nanostructured reduced activation and coarsen-grained steel irradiated to 2 dpa, which showed the sizes of 1.8–5.2 nm and 3.0–8.2 nm, respectively. Helium-ion irradiation can introduce the helium bubbles to the Cr-HEA and Zr-HEA like classic alloys, but mobility and following gather of the bubbles are suppressed due to the specialty of HEAs. Therefore, there seems to be no trace of a large bubble above 3 nm in the three irradiated specimens.

Fig. 9 shows the dislocation loops marked by white arrows in all irradiated specimens. To our knowledge, this is the first time to report the formation of dislocation loop in bcc-structure HEAs after irradiation. The three specimens show similar loop sizes about 4–6 nm, but the loop density has an obvious distinction that there

Table 3
Statistical results of dislocation of the Cr-HEA and Zr-HEA.

HEAs	Fluence (10^{17} ions/cm^2)	Mean size (nm)	Density (10^{21} m^{-3})
Cr-HEA	1	5.55	1.37
	5	5.66	2.13
Zr-HEA	5	5.67	2.40

are more loops in high-dose specimens than in low-dose specimens. Higher-dose irradiation only can induce more loops but does not influence the loop size. The reason is that severe lattice distortion in HEAs provides obstacles to the mobility of point defects. The statistical results about the mean size and density of the dislocation loops are summarized in Table 3. Only obvious loops are included, black spots and obscure loops are uniformly excluded. Fig. 10 shows the mean sizes of dislocation loops of conventional alloys from the literature [51–58]. Although there are some dislocation loops formed by the combination of interstitials in the two HEAs, the loops have a smaller size compared with conventional alloys.
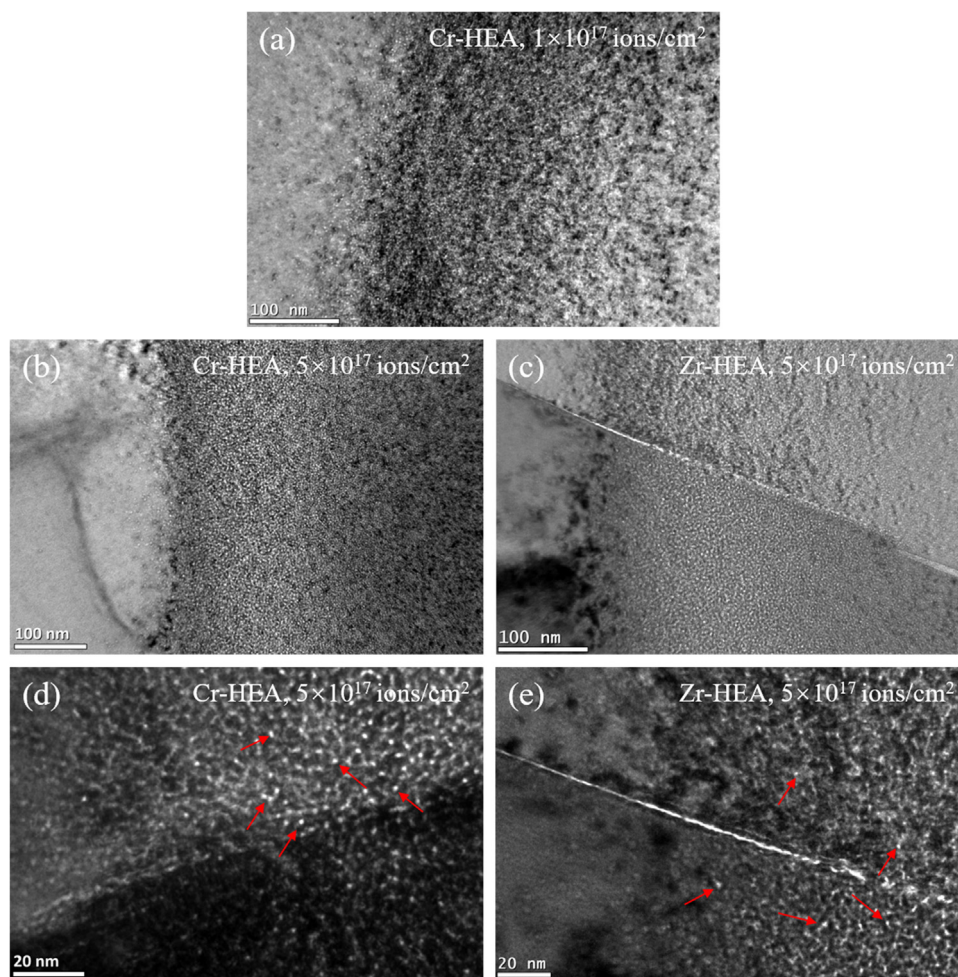
Fig. 8. Cross-section TEM BF images of the specimens irradiated by helium ion: (a) Cr-HEA at ion fluences of 1×10^{17} ions/cm^2, (b) Cr-HEA at ion fluences of 5×10^{17} ions/cm^2, (c) Zr-HEA at ion fluences of 5×10^{17} ions/cm^2. There are considerable small white spots that represent helium bubbles. High-magnification TEM BF images of helium bubbles: (d) Cr-HEA at ion fluences of 5×10^{17} ions/cm^2, (e) Zr-HEA at ion fluences of 5×10^{17} ions/cm^2. The helium bubbles are marked by red arrows.
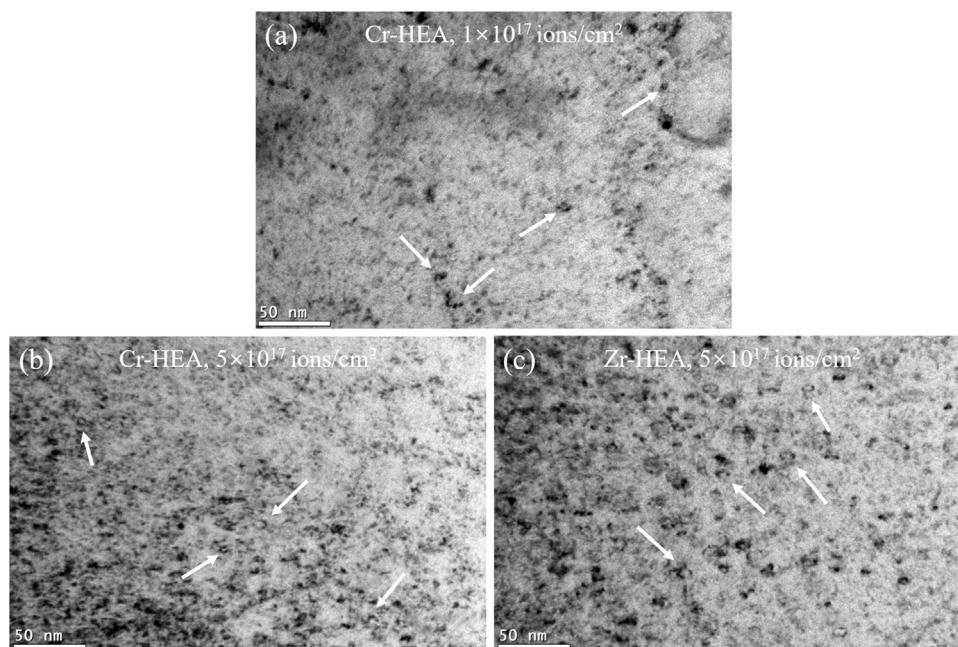
Fig. 9. Cross-section TEM BF images of the specimens irradiated by helium ion: (a) Cr-HEA at ion fluences of 1×10^{17} ions/cm^2, (b) Cr-HEA at ion fluences of 5×10^{17} ions/cm^2, (c) Zr-HEA at ion fluences of 5×10^{17} ions/cm^2. Some irradiated-induced dislocation loops are marked by white arrows.
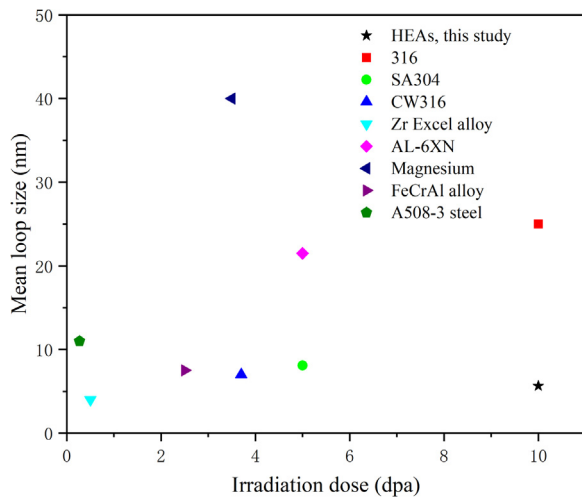
Fig. 10. Mean sizes of dislocation loops for conventional alloys from literature.

Several papers [59–61] have shown that irradiation hardening has a link with irradiation-induced microstructure evolution. The helium bubbles and dislocation loops are primary irradiation defects, which serve as obstacles to dislocation glide to induce hardening. The helium bubbles are too many to count, and they have less influence on hardening than the dislocation loops due to their smaller size. Therefore, only the dislocation loops are counted to establish the relation with irradiation hardening. The dispersed barrier hardening model has provided a reasonable correlation between irradiation hardening and dislocation loop, as follows [60]:

$$\Delta\sigma_y = M\alpha\mu b (dN)^{0.5} \tag{2}$$

where $\Delta\sigma_y$ is the yield strength increase value, M is the Taylor factor, α is the barrier strength factor, μ is the shear modulus, b is the Burgers vector of the gliding dislocations, d is the loop diameter (nm), and N is the loop density (m^{-3}). Higgy and Hammad showed a linear relationship between the yield stress and hardness, as follows [62]:

$$\Delta H = K\Delta\sigma_y \tag{3}$$

where K is variable for the different alloys. The larger the loop size and/or loop density, the higher the hardening. As shown in Table 3, the high-dose specimens have a larger density than the low-dose specimen, whereas the sizes of all specimens have a slight difference. Thus, high-dose irradiation induces larger hardening, which conforms to nanoindentation measurement results. Comparing the two HEAs irradiated to high dose, the Zr-HEA has a slightly larger loop density than the Cr-HEA. However, the Cr-HEA exhibits slightly larger irradiation hardening than the Zr-HEA. There may have two reasons that (1) the obscure loops are neglected, and (2) other defects such as bubbles and black spots also have a contribution to hardening. The post-irradiation hardness increases by 19.23 % and 19.18 % at 10.5 dpa relative to the original hardness for the Cr-HEA and Zr-HEA, respectively, which suggests that they may suffer from a similar level of irradiation damage.

Voids are generally observed in materials irradiated to dose above 1 dpa, due to the accumulation of irradiation-induced vacancies into stable cavities [63]. Voids can cause dimensional expansion and lead to degradation of fracture toughness [1]. Radiation-induced segregation (RIS) is the non-equilibrium segregation of alloying elements near sinks, which has been considered a primary cause of irradiation-assisted stress corrosion cracking [64]. However, no voids and RIS are observed in the three irradiated specimens. In the two HEAs, the severe lattice distortion can cause sluggish diffusion of irradiation-induced defects to suppress the formation of defect clusters, and the annihilation of defects can occur during the amorphization to crystallization process for high atomic-level stress [42,65]. Therefore, Cr-HEA and Zr-HEA may possess promising helium-ion irradiation resistance due to their stable crystal structure and slight microstructure evolution.

4. Conclusions

Aiming at ATF cladding, two novel bcc-structure $Mo_{0.5}NbTiVCr_{0.25}$ and $Mo_{0.5}NbTiV_{0.5}Zr_{0.25}$ HEAs composed of low thermal neutron cross-section elements were designed and prepared. Helium-ion irradiation was performed on the two HEAs, and the crystal structure, hardness, and microstructure evolution were investigated. These experimental results showed that the two HEAs may possess outstanding irradiation resistance and can be applicable for ATF cladding. The following conclusions could be drawn:

(1) The crystal structure of the Cr-HEA remains stable at low fluences of 1×10^{17} ions/cm², whereas the high fluences of 5×10^{17} ions/cm² cause the formation of an amorphous structure. However, the local melting and recrystallization of amorphous structure will occur due to thermal spikes induced by irradiation.

(2) The hardness increase of the Cr-HEA is 0.77 GPa at fluences of 1×10^{17} ions/cm² and 1.49 GPa at fluences of 5×10^{17} ions/cm², respectively. The hardness increase of the Zr-HEA is 1.36 GPa at fluences of 5×10^{17} ions/cm². The post-irradiation hardness increases by 19.23 % and 19.18 % relative to the original hardness for the Cr-HEA and Zr-HEA at high fluences, which exhibit less irradiation hardening compared with most of the conventional alloys.

(3) The sizes of helium bubbles and dislocation loops are about 1–3 and 4–6 nm at both fluences (2.1 and 10.5 dpa), respectively, which are smaller than classical alloys. The higher irradiation fluences can cause larger loop density, but do not influence the loop size, due to sluggish mobility of point defects.

(4) Voids and RIS are generally observed in irradiated materials. However, no voids and RIS are observed in the two HEAs irradiated to high fluences of 5×10^{17} ions/cm² (10.5 dpa), which indicates that the two HEAs may possess outstanding irradiation resistance.

Declaration of Competing Interest

The authors declare that they have no known competing financial interests or personal relationships that could have appeared to influence the work reported in this paper.

Acknowledgment

References

[1] S.J. Zinkle, G.S. Was, Acta Mater. 61 (2013) 735–758.
[2] R.M. Boothby, J. Nucl. Mater. 230 (1996) 148–157.
[3] A.F. Rowcliffe, L.K. Mansur, D.T. Hoelzer, R.K. Nanstad, J. Nucl. Mater. 392 (2009) 341–352.
[4] I. Charit, JOM 70 (2017) 1–3.
[5] Z. Duan, H. Yang, Y. Satoh, K. Murakami, S. Kano, Z. Zhao, J. Shen, H. Abe, Nucl. Eng. Des. 316 (2017) 131–150.
[6] K.A. Terrani, S.J. Zinkle, L.L. Snead, J. Nucl. Mater. 448 (2014) 420–435.
[7] S.J. Zinkle, K.A. Terrani, L.L. Snead, Curr. Opin. Solid State Mater. Sci. 20 (2016) 401–410.
[8] A.T. Motta, L.Q. Chen, JOM 64 (2012) 1403–1408.

[9] K.A. Terrani, J. Nucl. Mater. 501 (2018) 13–30.

[10] S.J. Zinkle, K.A. Terrani, J.C. Gehin, L.J. Ott, L.L. Snead, J. Nucl. Mater. 448 (2014) 374–379.

[11] J.W. Yeh, S.K. Chen, S.J. Lin, J.Y. Gan, T.S. Chin, T.T. Shun, C.H. Tsau, S.Y. Chang, Adv. Eng. Mater. 6 (2004) 299–303.

[12] B. Cantor, I.T.H. Chang, P. Knight, A.J.B. Vincent, Mater. Sci. Eng. A 375-377 (2004) 213–218.

[13] W. Zhang, P.K. Liaw, Y. Zhang, Sci. China Mater. 61 (2018) 2–22.

[14] Y. Zhang, T.T. Zuo, Z. Tang, M.C. Gao, K.A. Dahmen, P.K. Liaw, Z.P. Lu, Prog. Mater. Sci. 61 (2014) 1–93.

[15] Y.F. Ye, Q. Wang, J. Lu, C.T. Liu, Y. Yang, Mater. Today 19 (2016) 349–362.

[16] D.B. Miracle, O.N. Senkov, Acta Mater. 122 (2017) 448–511.

[17] B. Gludovatz, A. Hohenwarter, D. Catoor, E.H. Chang, E.P. George, R.O. Ritchie, Science 345 (2014) 1153–1158.

[18] Y. Zou, H. Ma, R. Spolenak, Nat. Commun. 6 (2015) 7748.

[19] O.N. Senkov, J.M. Scott, S.V. Senkova, D.B. Miracle, C.F. Woodward, J. Alloys Compd. 509 (2011) 6043–6048.

[20] C. Xiang, J. Wang, H. Fu, E.H. Han, Z. Zhang, J. Chin. Soc. Corros. Prot. 36 (2016) 107–112.

[21] Y.Y. Chen, U.T. Hong, H.C. Shih, J.W. Yeh, T. Duval, Corros. Sci. 47 (2005) 2679–2699.

[22] H. Luo, Z. Li, A.M. Mingers, D. Raabe, Corros. Sci. 134 (2018) 131–139.

[23] S. Shuang, Z.Y. Ding, D. Chung, S.Q. Shi, Y. Yang, Corros. Sci. 164 (2020) 108315.

[24] F. Otto, A. Dlouhý, C. Somsen, H. Bei, G. Eggeler, E.P. George, Acta Mater. 61 (2013) 5743–5755.

[25] Z. Wu, Y. Gao, H. Bei, Acta Mater. 120 (2016) 108–119.

[26] Y. Zhang, M.A. Tunes, M.L. Crespillo, F. Zhang, W.L. Boldman, P.D. Rack, L. Jiang, C. Xu, G. Greaves, S.E. Donnelly, L. Wang, W.J. Weber, Nanotechnology 30 (2019) 294004.

[27] A. Poulia, E. Georgatis, A. Lekatou, A.E. Karantzalis, Int. J. Refract. Met. Hard Mater. 57 (2016) 50–63.

[28] M.H. Chuang, M.H. Tsai, W.R. Wang, S.J. Lin, J.W. Yeh, Acta Mater. 59 (2011) 6308–6317.

[29] Y. Yu, J. Wang, J. Li, J. Yang, H. Kou, W. Liu, J. Mater. Sci. Technol. 32 (2016) 470–476.

[30] N.A.P.K. Kumar, C. Li, K.J. Leonard, H. Bei, S.J. Zinkle, Acta Mater. 113 (2016) 230–244.

[31] L. Yang, H. Ge, J. Zhang, T. Xiong, Q. Jin, Y. Zhou, X. Shao, B. Zhang, Z. Zhu, S. Zheng, X. Ma, J. Mater. Sci. Technol. 35 (2019) 300–305.

[32] Y. Lu, H. Huang, X. Gao, C. Ren, J. Gao, H. Zhang, S. Zheng, Q. Jin, Y. Zhao, C. Lu, T. Wang, T. Li, J. Mater. Sci. Technol. 35 (2019) 369–373.

[33] P.L. Andresen, G.S. Was, in: R.J.M. Konings (Ed.), Comprehensive Nuclear Materials, Elsevier, Oxford, 2012, pp. 177–205.

[34] T. Egami, M. Ojha, O. Khorgolkhuu, D.M. Nicholson, G.M. Stocks, JOM 67 (2015) 2345–2349.

[35] M. Moschetti, A. Xu, B. Schuh, A. Hohenwarter, J.P. Couzinié, J.J. Kruzic, D. Bhattacharyya, B. Gludovatz, JOM 72 (2019) 130–138.

[36] C. Xiang, E.H. Han, Z.M. Zhang, H.M. Fu, J.Q. Wang, H.F. Zhang, G.D. Hu, Intermetallics 104 (2019) 143–153.

[37] C. Xiang, H.M. Fu, Z.M. Zhang, E.H. Han, H.F. Zhang, J.Q. Wang, G.D. Hu, J. Alloys Compd. 818 (2020) 153352.

[38] L. Vegard, Zeitschrift für Physik 5 (1921) 17–26.

[39] Y. Long, K. Su, J. Zhang, X. Liang, H. Peng, X. Li, Materials 11 (2018) 669.

[40] S. Sun, N. Qiu, K. Zhang, P. He, Y. Ma, F. Gou, Y. Wang, Scr. Mater. 161 (2019) 40–43.

[41] H. Jiang, Z. Duan, X. Zhao, B. Zhang, P. Wang, Appl. Surf. Sci. 498 (2019) 143821.

[42] T. Egami, W. Guo, P.D. Rack, T. Nagase, Metall. Mater. Trans. A 45 (2013) 180–183.

[43] T.Y. Tsui, G.M. Pharr, J. Mater. Res. 14 (2012) 292–301.

[44] S.J. Zinkle, J.T. Busby, Mater. Today 12 (2009) 12–19.

[45] X. Zhang, C. Zhang, Z. Ding, Y. Chen, L. Zhang, J. Nucl. Mater. 531 (2020) 152014.

[46] Y. Liu, W. Liu, L. Yu, L. Chen, H. Sui, H. Duan, Crystals 10 (2020) 44.

[47] X. Bai, S. Wu, P. Liaw, L. Shao, J. Gigax, Metals 7 (2017) 25.

[48] C. Xu, L. Zhang, W. Qian, J. Mei, X. Liu, Nucl. Eng. Technol. 48 (2016) 758–764.

[49] G. Lei, R. Xie, H. Huang, R. Liu, Q. Huang, J. Li, Y. Zhou, C. Li, Q. Lei, Q. Deng, Y. Wang, C. Wang, W. Zhang, L. Yan, M. Tang, J. Alloys Compd. 746 (2018) 153–158.

[50] W.B. Liu, J.H. Zhang, Y.Z. Ji, L.D. Xia, H.P. Liu, D. Yun, C.H. He, C. Zhang, Z.G. Yang, J. Nucl. Mater. 500 (2018) 213–219.

[51] J. Gan, E.P. Simonen, S.M. Bruemmer, L. Fournier, B.H. Sencer, G.S. Was, J. Nucl. Mater. 325 (2004) 94–106.

[52] A. Etienne, M. Hernández-Mayoral, C. Genevois, B. Radiguet, P. Pareige, J. Nucl. Mater. 400 (2010) 56–63.

[53] H.F. Huang, J.J. Li, D.H. Li, R.D. Liu, G.H. Lei, Q. Huang, L. Yan, J. Nucl. Mater. 454 (2014) 168–172.

[54] X.H. Li, J. Lei, G.G. Shu, Q.M. Wan, Methods Phys. Res. Sect. B 350 (2015) 14–19.

[55] Z.C. Zheng, Y.X. Yu, W.P. Zhang, Z.Y. Shen, F.F. Luo, L.P. Guo, Y.Y. Ren, R. Tang, Acta Metall. Sin. (Engl. Lett.) 30 (2016) 89–96.

[56] J.C. Haley, S.A. Briggs, P.D. Edmondson, K. Sridharan, S.G. Roberts, S. Lozano-Perez, K.G. Field, Acta Mater. 136 (2017) 390–401.

[57] H. Yu, Z. Yao, Y. Idrees, H.K. Zhang, M.A. Kirk, M.R. Daymond, J. Nucl. Mater. 491 (2017) 232–241.

[58] Q. Dong, Z. Yao, P. Saidi, M.R. Daymond, J. Nucl. Mater. 511 (2018) 43–55.

[59] B.N. Singh, A.J.E. Foreman, H. Trinkaus, J. Nucl. Mater. 249 (1997) 103–115.

[60] S.J. Zinkle, Y. Matsukawa, J. Nucl. Mater. 329-333 (2004) 88–96.

[61] C.R.F. Azevedo, Eng. Failure Anal. 18 (2011) 1921–1942.

[62] H.R. Higgy, F.H. Hammad, J. Nucl. Mater. 55 (1975) 177–186.

[63] B.N. Singh, S.J. Zinkle, J. Nucl. Mater. 206 (1993) 212–229.

[64] H. Wiedersich, P.R. Okamoto, N.Q. Lam, J. Nucl. Mater. 83 (1979) 98–108.

[65] S.Q. Xia, Z. Wang, T.F. Yang, Y. Zhang, J. Iron Steel Res. Int. 22 (2015) 879–884.